Extending the Harmonic Optimization Function of Capacitively Coupled Active Damper for LCL-Equipped High-Speed PMSM Drives

Jiaxin Zhou, *Student Member, IEEE*, Yunkai Huang, Fei Peng, and Yu Yao, *Member, IEEE*

***Abstract*—This article extends the harmonic optimization capabilities of capacitively coupled active dampers for LCL-equipped high-speed permanent magnet synchronous drives. The benefit of the proposed approach is that the active damper not only provides resonance damping but also reduces the harmonics of the motor current. The resonant damping loop is implemented by feeding the motor current in series with a high-pass filter. The harmonic optimization loop is implemented by capacitor voltage feedback. Compared with the traditional current-type active damper, the capacitive-coupled active damper has a simpler topology, lower dc voltage stress, lower loss, and simpler control structure. The proposed extended harmonic optimization method has been experimentally demonstrated to reduce the motor current harmonics by approximately 25%.**

***Index Terms*—Active damper, high-speed permanent magnet synchronous motor (HSPMSM), harmonic optimization, LCL filter, resonance suppression.**

I. Introduction

TO FURTHER improve the power density and dynamic performance of the motor drives, the upper limit of the motor speed has been gradually increased, and high-speed permanent magnet synchronous motors (HSPMSM) have received more and more attention [1].

A. LCL Filter and HSPMSM Drives

However, the high fundamental frequency and low inductance characteristics of HSPMSM lead to large harmonics in the motor current [2]. High harmonic stator current increases the high-frequency (HF) loss of the motor, making the already difficult heat dissipation problem even more difficult. In addition, high dv/dt increases the electromagnetic interference and voltage stress requirements of the drives [3].

Received 12 July 2024; revised 6 September 2024; accepted 26 October 2024. Date of publication 29 October 2024; date of current version 18 December 2024. This work was supported in part by the National Natural Science Foundation of China under Grant 52277036 and Grant 52277037, and in part by the Natural Science Foundation of Jiangsu Province under Grant BK20241321. Recommended for publication by Associate Editor R. Kennel. *(Corresponding author: Yunkai Huang.)*

The authors are with the School of Electrical Engineering, Southeast University, Nanjing 210096, China (e-mail: jxzhou1996@seu.edu.cn; huangyk@seu.edu.cn; pengfei@seu.edu.cn; yuyao@seu.edu.cn).

Color versions of one or more figures in this article are available at https://doi.org/10.1109/TPEL.2024.3487843.

Digital Object Identifier 10.1109/TPEL.2024.3487843

An LCL filter is an effective means to solve these problems. However, the resonance damping of LCL filter has become a new problem. In HSPMSM drives, the resonant frequency in dq synchronous coordinates varies with the fundamental frequency over a wide range, resulting in greater difficulty in resonant damping of HSPMSM than that of grid-connected inverters [4].

B. Existing Damping Methods

The traditional passive damping (PD) method requires an additional hardware damping network, and its loss is large in HSPMSM drive [5]. Compared with the PD methods, the active damping (AD) methods do not require additional hardware damping network and with lower losses. The AD methods mainly includes filter-based [6], [7], inherent damping [8], virtual-resistance [9], [10], [11], full state feedback control (FSFC) [12], and hybrid damping [13], [14]. The FSFC method can realize the free configuration of system poles, but requires a large number of additional sensors. Furthermore, to save sensors, state observer-based methods [15] and single-sensor damping methods are proposed [16].

It is undeniable that the AD method has the simplest hardware structure. However, according to Shannon's sampling theorem, the resonant frequency of the system cannot be higher than half the sampling frequency, which is the Nyquist frequency. It is imperative to keep the crossover frequency as low as possible to ensure effective damping. So, the Nyquist frequency should be considered as the upper limit for the filter's crossover frequency, even with the advanced AD control methods [4]. Otherwise, the resonant component will be missampled as signals of other frequencies.

Consequently, limited by the upper resonant frequency limit, the passive components of the filter must be large, resulting in an increase in the filter's size. Moreover, to achieve reliable damping, the HSPMSM driver must operate in a fixed switching frequency mode, which restricts the use of changing switching frequency control strategy to reduce losses. In addition, existing AD methods are susceptible to system parameter mismatch. However, the parameters of HSPMSM drives are elementary to change during operation, which reduces the reliability of these AD methods [17], [18].

TABLE I
SUMMARY OF EXISTING DAMPING METHODS

	Cons	Pros
PD in [5]	Additional hardware, high power loss.	No resonant frequency limit, strong robustness.
AD in [32]	Low upper resonance frequency and robustness.	No additional hardware, low power loss.
Series damper in [19]	High current stress, large devices quantity.	Low switching frequency, strong robustness.
Inductively coupled damper [23]	High voltage stress and loss.	Low current stress, strong robustness.
Capacitively coupled damper in [27]	Limited improvement in voltage stress and losses.	Relatively reduce voltage stress and loss.
Capacitively coupled damper in [31]	Active harmonic mitigation is not considered.	Low loss and voltage stress, simple control structure.

C. Existing Active Dampers

To overcome the shortcomings of the AD method, active dampers [19] are proposed.

In [19], the active damper is connected in series in the load loop. The current stress of the series active damper is the same as that of the main inverter and requires a large number of switching devices. The parallel current-controlled (inductively coupled) active dampers have been applied to the resonance suppression of multiple-inverter grid-connected systems [20], [21], [22], [23], [24], [25]. However, the current-controlled active damper requires additional current sensors and a high-bandwidth current controller, which places extremely high demands on the performance of the microcontroller unit. What is more, the voltage stress of this type of active damper is relatively large, which is consistent with that of the main inverter, resulting in extremely high switching losses.

In order to reduce the voltage stress and loss of the damper, capacitivly coupled active damper is proposed. In [26], capacitive coupling damper is used for disturbance suppression in ac power-electronics-based power systems. The dc voltage of the damper and the inverter is 300 and 750 V, respectively. The authors of [27], [28], and [29] used capacitively coupled damper to suppress the current harmonics of high-power inverters, but they need additional current sensors. Moreover, the voltage and current stress of the auxiliary converter are still high, 200 V for the damper and 730 V for the main-inverter. Zhou et al. [30] applied a capacitively coupled active damper to solve the resonance problem of an LCL-equipped HSPMSM drives, the voltage stress of the damper was reduced to 5% of the main inverter dc voltage. Furthermore, in [31], a single-motor-current-feedback control strategy with adaptive feedback gain was proposed to simplify the system structure.

D. Proposed Method

Table I lists the advantages and disadvantages of existing AD methods. To summarize, the PD method has high losses, the AD method has a small effective resonant frequency range, the series damper has a large capacity and a large number of components, the inductively coupled active damper has high voltage stress and switching losses, and the capacitively coupled active damper excels in voltage stress, loss and system complexity. The control method of [31] greatly reduces the loss and cost of the capacitive coupling active damper, and are expected to be applied in engineering. However, the active harmonic suppression function of the active damper was not considered.

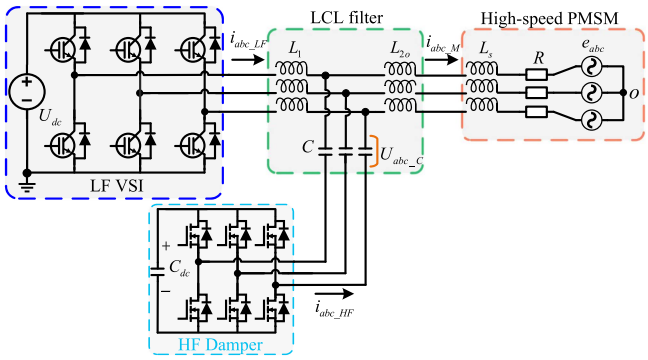

Fig. 1. System structure of LCL-equipped HSPMSM drives with capacitively coupled active damper.

In view of this, this article further extends the harmonic optimization function on the basis of [31] to further reduce the motor current harmonics and improve the efficiency of the HSPMSM system. The state feedback of the capacitor voltage is introduced to suppress the sideband harmonics of the motor current. Finally, the effectiveness of the proposal are validated by experiments.

II. RESONANCE DAMPING BASED ON CAPACITIVELY COUPLED ACTIVE DAMPER

The system diagram of LCL-HSPMSM drives with active damper are shown in Fig. 1. The system consists of a low-frequency voltage source inverter (LF-VSI), LCL filter, HSPMSM, and high-frequency damper (HF-Damper). R denotes the motor resistance, L_s denotes the motor inductance, e_{abc} denotes the motor back electromotive force. i_{abc_LF}, i_{abc_HF}, and i_{abc_M} are the LF-VSI current, HF-Damper current and motor current, respectively. U_{abc_C} represents the capacitor voltage. The inverter side filter inductor L_1, the motor side filter inductor L_{2o} and the filter capacitor C together form the LCL filter. The definitions and values of relevant variables are shown in Table II, and L_2 is defined as the sum of L_{2o} and L_s.

A. System Model With Capacitively Coupled Active Damper

To simplify modeling, the following assumptions are made.

1) e_{abc} changes slowly and compensated by feedforward.
2) R is small and has no negative effect on resonance.
3) The HF-Damper switching frequency is much higher than that of the LF-VSI.

TABLE II
PARAMETERS OF THE EXPERIMENTAL PLANT

Symbol	Parameter	Value
R	motor resistance	0.05 Ω
L_s	motor inductance (SPMSM)	220 μH
L_1	LCL filter inverter side inductance	100 μH
L_2o	LCL filter motor side inductance	0 μH
C	LCL filter capacitance	8 μF
$C_{\rm dc}$	HF-Damper dc link capacitance	32 μF
$f_{\rm res}$	LCL filter resonant frequency	6786 Hz
poles	poles of the HSPMSM	10
$f_{\rm LF}/T_{\rm LF}$	LF-VSI switching frequency/period	10 kHz/100 μs
$f_{\rm HF}/T_{\rm HF}$	HF-Damper switching frequency/period	100 kHz/10 μs
f_N	motor rated fundamental frequency	1000 Hz
$V_{\rm dc}$	LF-VSI dc link voltage	300 V
$V^*_{\rm dc2}$	HF-Damper dc link voltage reference	30 V
I_N	motor rated current	14 A
U_N	motor rated voltage	130 V
P_N	motor rated power	3 kW

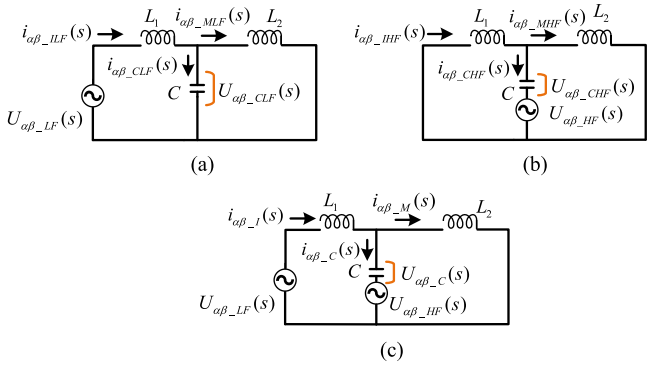

Fig. 2. Single-phase equivalent circuit based on superposition theorem. (a) LF-VSI part. (b) HF-Damper part. (c) Overall.

According to the superposition theorem, the single-phase equivalent circuit of LCL-equipped HSPMSM drives with active damper is depicted in Fig. 2. $U_{\alpha\beta\_\rm LF}(s)$ and $U_{\alpha\beta\_\rm HF}(s)$ are LF-VSI output voltage complex vector and HF-Damper output voltage complex vector, respectively. The complex vectors $i_{\alpha\beta\_I}(s)$, $i_{\alpha\beta\_M}(s)$, $i_{\alpha\beta\_C}(s)$ denote the inverter current, motor current and capacitor current complex vector, respectively. $i_{\alpha\beta\_\rm ILF}(s)$, $i_{\alpha\beta\_\rm MLF}(s)$, $i_{\alpha\beta\_\rm CLF}(s)$, and $U_{\alpha\beta\_\rm CLF}(s)$ denote the inverter current, motor current, capacitor current and capacitor voltage complex vector under the action of LF-VSI only, respectively. $i_{\alpha\beta\_\rm IHF}(s)$, $i_{\alpha\beta\_\rm MHF}(s)$, $i_{\alpha\beta\_\rm CHF}(s)$, and $U_{\alpha\beta\_\rm CLF}(s)$ denote the inverter current, motor current, capacitor current, and capacitor voltage complex vector under the action of HF-Damper only, respectively.

The superposition model shown in Fig. 2 can be represented by the signal flow graph shown in Fig. 3, where $G_{uc1}(s)$, $G_{iM1}(s)$, $G_{uc2}(s)$, and $G_{iM2}(s)$ are defined as

$$G_{uc1}(s) = \frac{sL_2}{s^3L_1L_2C + s(L_1+L_2)}$$

$$G_{iM1}(s) = \frac{1}{sL_2}$$

$$G_{uc2}(s) = \frac{-s(L_1+L_2)}{s^3L_1L_2C + s(L_1+L_2)}$$

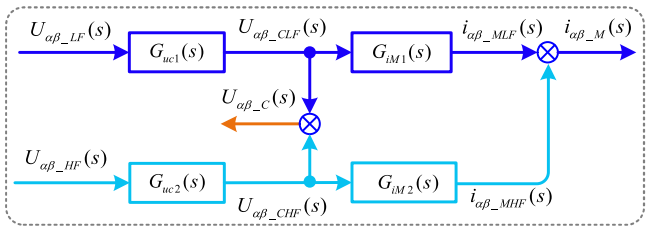

Fig. 3. Dual-source equivalent structure block diagram with active damper.

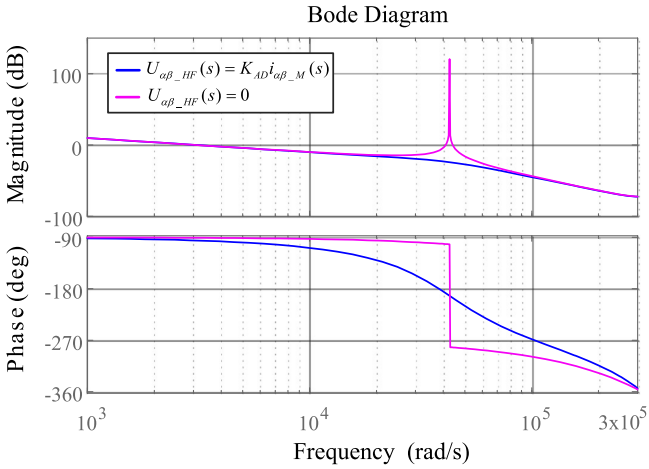

Fig. 4. Bode diagram of $G_{iM}(s)$ with different $U_{\alpha\beta\_\rm HF}(s)$.

$$G_{iM2}(s) = -\frac{sL_1C}{L_1+L_2}. \tag{1}$$

According to Fig. 3, the expression of the capacitor voltage $U_{\alpha\beta\_C}(s)$ in the $\alpha\beta$ stationary coordinate is

$$U_{\alpha\beta\_C}(s) = G_{uc1}(s)U_{\alpha\beta\_\rm LF}(s) + G_{uc2}(s)U_{\alpha\beta\_\rm HF}(s). \tag{2}$$

The expression of the motor current $i_{\alpha\beta\_M}(s)$ in the $\alpha\beta$ stationary coordinate is

$$\begin{aligned} i_{\alpha\beta\_M}(s) = {} & G_{uc1}(s)G_{iM1}(s)U_{\alpha\beta\_\rm LF}(s) \\ & + G_{uc2}(s)G_{iM2}(s)U_{\alpha\beta\_\rm HF}(s). \end{aligned} \tag{3}$$

If $U_{\alpha\beta\_\rm HF}(s)$ is zero, the system is equivalent to an undamped LCL-equipped HSPMSM drives, and the transfer function from the motor current to the LF-VSI output voltage is

$$G_{iM}(s) = \frac{i_{\alpha\beta\_M}(s)}{U_{\alpha\beta\_\rm LF}(s)} = \frac{1}{s^3L_1L_2C + s(L_1+L_2)}. \tag{4}$$

As illustrated in Fig. 4, when $U_{\alpha\beta\_\rm HF}(s)$ is zero, the Bode diagram reveals that the system is afflicted with a resonance problem. The resonant angular frequency $\omega_{\rm res}$ and resonant frequency $f_{\rm res}$ are defined as

$$\omega_{\rm res} = 2\pi f_{\rm res} = \sqrt{\frac{L_1+L_2}{L_1L_2C}}. \tag{5}$$

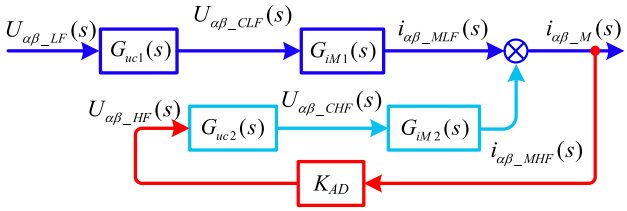

Fig. 5. System block diagram with resonance damping only.

B. Damping Principle of Active Damper

From the above-mentioned analysis, it can be seen that it is possible to achieve resonance suppression by setting $U_{\alpha\beta\_\mathrm{HF}}(s)$ reasonably. To suppress the resonance, try setting $U_{\alpha\beta\_\mathrm{HF}}(s)$ as

$$U_{\alpha\beta\_\mathrm{HF}}(s) = K_{\mathrm{AD}} i_{\alpha\beta\_M}(s). \tag{6}$$

Subsequently, the signal flow diagram of the system can be expressed in the form of Fig. 5.

Furthermore, simplifying the control structure shown in Fig. 5, the transfer function from the motor current to the LF-VSI output voltage is

$$\begin{aligned} G_{iM}(s) &= \frac{G_{uc1}(s)G_{iM1}(s)}{1 - G_{uc2}(s)G_{iM2}(s)K_{\mathrm{AD}}} \\ &= \frac{1}{s^3 L_1 L_2 C + s(L_1 + L_2) - s^2 L_1 C K_{\mathrm{AD}}}. \end{aligned} \tag{7}$$

The Bode diagram of the system with active damper is depicted in Fig. 4. The Bode plot shows that the application of active dampers has a significant effect on suppressing the resonance peak.

According to (10)–(16) in [31], the extreme values of the feedback gain K_{AD} are

$$\begin{aligned} K_{\mathrm{AD\_Min}} &= -2L_2 s\omega_{\mathrm{res}} \\ K_{\mathrm{AD\_Max}} &= -L_2/(L_1 + L_2). \end{aligned} \tag{8}$$

In generally, the value of K_{AD} can set between $K_{\mathrm{AD\_Min}}$ and $K_{\mathrm{AD\_Max}}$. Without loss of generality, the recommended K_{AD} is

$$K_{\mathrm{AD}} = \frac{K_{\mathrm{AD\_Max}} + K_{\mathrm{AD\_Min}}}{2}. \tag{9}$$

C. Implementation of Damping Based on Active Damper

The block diagram of the resonance damping method based on capacitive coupling damper is shown in Fig. 6, where Fig. 6(a) is the low-frequency (LF) motor control block diagram, and Fig. 6(b) is the HF damper control block diagram. The transformation matrix from abc stationary coordinate to dq synchronous coordinate is represented by T_{abc2dq}, while the transformation matrix from dq synchronous coordinate to abc stationary coordinate is represented by T_{dq2abc}.

In Fig. 6(a), i_{dq_M} represents the motor current complex vector in dq synchronous coordinate, U_{dq_LF} represents the output voltage of the HF-Damper in dq synchronous coordinate, and U_{abc_LF} represents the output voltage of the HF-Damper in the abc stationary coordinate.

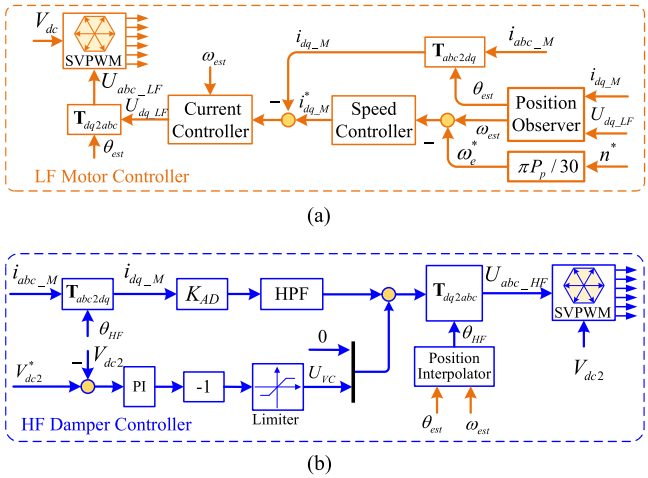

Fig. 6. Block diagram of resonance damping method based on capacitive coupling damper. (a) LF motor controller. (b) HF dmaper controller.

The design of the position observer can refer to [33], θ_{est} and ω_{est} are the estimated rotor position and angular frequency, respectively.

The speed controller is a proportional integral controller. n^* represents the reference speed, ω_e^* represents the electrical angular frequency, and $i^*_{dq\_\mathrm{LF}}$ is the output of the speed controller, that is, the current reference. The proportional and integral coefficients K_{pS} and K_{iS} are 0.01 and 0.02, respectively.

The current controller is defined as

$$G_c(z) = \frac{(az + b)(ze^{j\omega_e T} - e^{-RT/L_2})}{(z - 1)^2} \tag{10}$$

where a and b are control coefficients in [4].

In Fig. 6(b), U_{abc_HF} represents the output voltage of the HF-Damper in the abc stationary coordinate. In order to filter out the LF signals in the feedback current, a high-pass filter (HPF) is connected in series in the resonant damping loop.

First, the HPF is designed in the continuous domain, and its transfer function is

$$G_{\mathrm{HPF}}(s) = \frac{s}{s + \omega_c} \tag{11}$$

where the cutoff frequency ω_c is set as

$$\omega_c = 1.5\omega_{eN} \tag{12}$$

where ω_{eN} is motor rated angular frequency (2000π rad).

Then, the forward Euler discretization method is used to discretize (11) to obtain the discrete transfer function

$$G_{\mathrm{HPF}}(z) = \frac{T_{\mathrm{HF}}\omega_c}{z - 1 + T_{\mathrm{HF}}\omega_c} \tag{13}$$

where T_{HF} is the sampling period of HF-Damper.

The rotor position θ_{HF} is recursively derived from the θ_{est} and ω_{est}. The position interpolator is

$$\theta_{\mathrm{HF}} = \theta_{\mathrm{est}} + (k - 1)\omega_{\mathrm{est}} T_{\mathrm{HF}}, (k = 1, 2, 3 \ldots 10) \tag{14}$$

where k represents the kth HF period within an LF period, which can be found in Fig. 7.

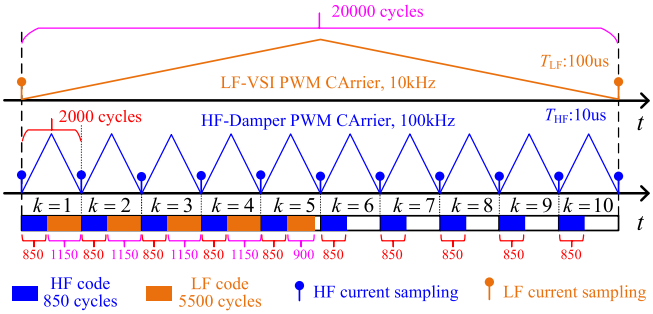

Fig. 7. Timing diagram of the control algorithm for the LCL-equipped HSPMSM drives with capacitively coupled active damper.

The dc link voltage of the damper is controlled by the PI controller shown in Fig. 6(b), where V_{dc2}^{*} is the voltage reference, U_{VC} is the output. The design basis of the proportional and integral coefficients K_{pV} and K_{iV} are as follows:

$$\begin{aligned} K_{pV} &= 2\pi f_b C_{\mathrm{dc}} \\ K_{iV} &= 2\pi f_b R_{\mathrm{eq}} \end{aligned} \tag{15}$$

where f_b is control bandwidth, C_{dc} is damper dc-link capacitance, and R_{eq} is equivalent resistance in the charging circuit.

The output limits of the voltage controller are $V_{\mathrm{dc2}}/6$ and $-V_{\mathrm{dc2}}/6$, respectively.

The timing diagram of the control algorithm is shown in Fig. 7. The starting point of the LF carrier is aligned with the starting point of the first HF carrier. The current sampling points of the LF-VSI and the HF-Damper are both the starting points of their carriers. The programs of the damper controller belong to HF code and the programs of the motor controller belongs to LF code. The number of operation cycles required to execute the HF code and the LF code is approximately 850 and 5500, respectively. In the HF period, the HF code is executed first. Then, if the LF code is not executed, jumps to the interrupt of the LF code.

III. Proposed Harmonic Optimization Method

A. Harmonic Optimization Principle

To extend the harmonic optimization function, in this article, the capacitor voltage is fed back into the reference voltage of the HF-Damper. Fig. 8 is the schematic diagram of the proposed harmonic optimization method, where K_C is the harmonic optimization coefficient, and the simplified system model is shown in Fig. 8(b). It should be pointed out that in order to facilitate the description of the proposed harmonic optimization method, the resonance damping of the HF-Damper will be discussed in the next section.

In the proposed harmonic optimization method, the output voltage of the HF-Damper is set as

$$U_{\alpha\beta\_\mathrm{HF}}(s) = K_C U_{\alpha\beta\_C}(s). \tag{16}$$

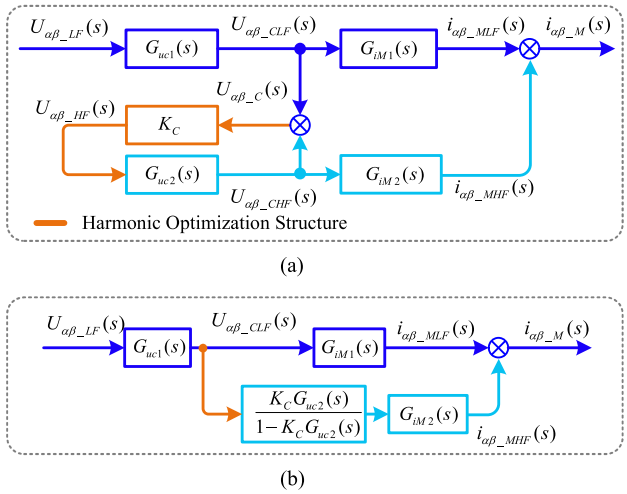

Fig. 8. System block diagram with proposed harmonic optimization only. (a) Original model. (b) Simplified model.

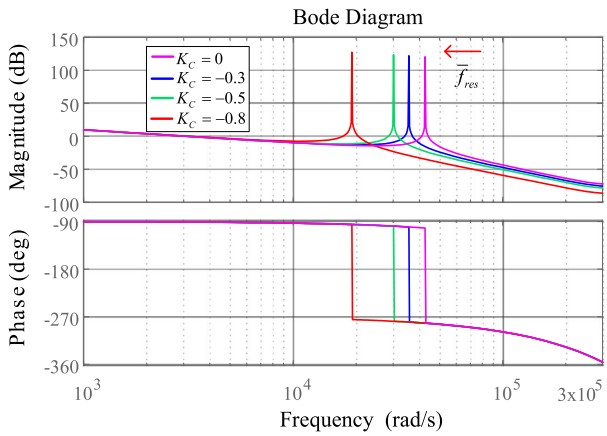

Fig. 9. Bode diagram of $G_{i\mathrm{MH}}(s)$ with different K_C.

Then, the transfer function from the motor current to the LF-VSI output voltage with harmonic optimization is

$$\begin{aligned} G_{i\mathrm{MH}}(s) &= G_{uc1}(s)[G_{iM1}(s) \\ &\quad + \frac{K_C G_{uc2}(s)}{1 - K_C G_{uc2}(s)} G_{iM2}(s)] \\ &= \frac{1 + K_C}{s^3 L_1 L_2 C + s(L_1 + L_2)(1 + K_C)}. \end{aligned} \tag{17}$$

The Bode diagram of $G_{i\mathrm{MH}}(s)$ is shown in Fig. 9. It can be seen that, when $K_C = 0$, the system model is consistent with (4), the HF attenuation capability of the system is not improved. If K_C gradually decreases from 0, the resonance peak of the system gradually shifts to the left, the equivalent resonant frequency of the system gradually decreases.

The equivalent resonant frequency and angular frequency of the system can be expressed as

$$\begin{aligned} \bar{f}_{\mathrm{res}} &= \sqrt{1 + K_C} f_{\mathrm{res}} \\ \bar{\omega}_{\mathrm{res}} &= \sqrt{1 + K_C} \omega_{\mathrm{res}}. \end{aligned} \tag{18}$$

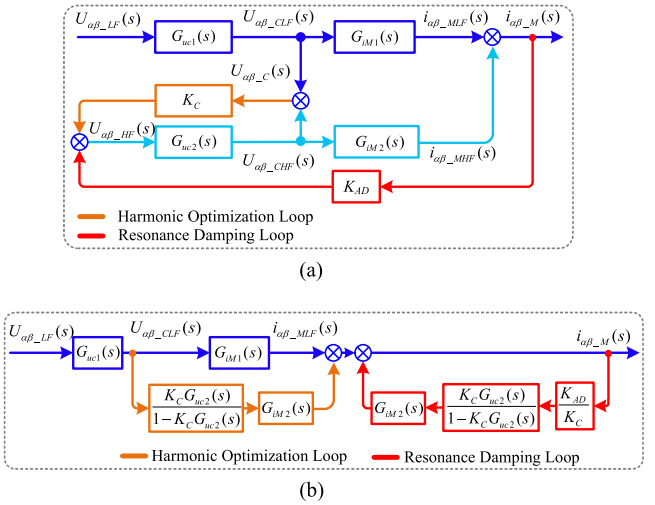

Fig. 10. System block diagram with proposed harmonic optimization and resonance damping. (a) Original model. (b) Simplified model.

The reduction of the equivalent resonant frequency reduces the HF gain of the system, thereby optimizing the HF harmonics of the system.

B. Design of Damping Controller With Harmonic Optimization

In the previous sections, the principles of resonance damping and harmonic optimization have been introduced, respectively. In this section, how to achieve these two functions at the same time will be discussed.

The system block diagram with proposed harmonic optimization and resonance damping is shown in Fig. 10, and the simplified model is shown in Fig. 10(b). According to the simplified model, the transfer function from the motor current to the LF-VSI output voltage with harmonic optimization and resonance damping is

$$G_{i\mathrm{MF}}(s) = G_{i\mathrm{MH}}(s)\frac{1}{1 - G_{iM2}(s)\frac{K_{\mathrm{AD}}G_{uc2}(s)}{1-K_C G_{uc2}(s)}} = \frac{1+K_C}{s^3 L_1 L_2 C + s(L_1+L_2)(1+K_C) - s^2 L_1 C K_{\mathrm{AD}}}. \quad (19)$$

The Bode plot of the system transfer function considering both resonant damping and harmonic optimization is shown in Fig. 11. It can be seen that based on the proposed method, resonance damping and harmonic optimization can be achieved simultaneously.

The final control block diagram of the method proposed is shown in Fig. 12. U_{abc_C} represents the capacitor voltage in the abc stationary coordinate, U_{dq_C} represents the capacitor voltage complex vector in dq synchronous coordinate. The same as Fig. 6(b), the LF signals in the motor current and capacitor voltage need to be filtered out. The parameters of the HPF can be found in (11) and (12)

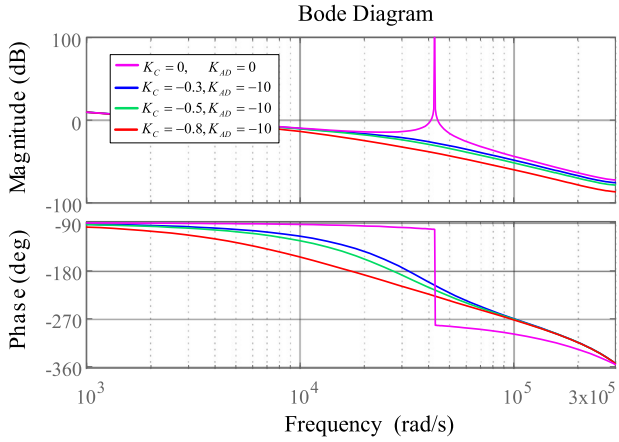

Fig. 11. Bode diagram of $G_{i\mathrm{MF}}(s)$ with different K_C.

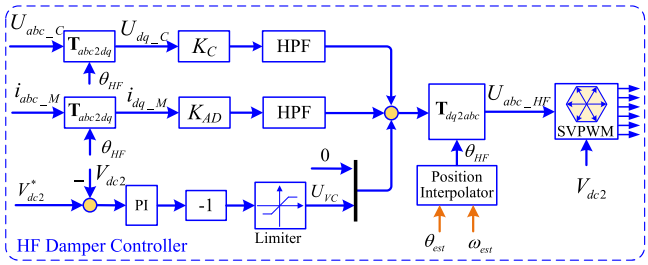

Fig. 12. Final damper control structure of the proposed method.

C. Analysis of the Impact of HPF

As shown in Fig. 12, in order to reduce the damper output voltage, HPFs are added to the harmonic optimization loop and the resonant damping loop. Therefore, it is necessary to consider the impact of the HPF.

Considering the HPF, the system transfer function can be expressed as (20), shown at the bottom of the next page. As shown in Fig. 13, for the systems with and without HPF, the LF and HF amplitude gains are almost the same, and the midfrequency gain in the system with HPF is slightly larger than that in the system without HPF. In addition, the phase margin of the system with HPF is greater than that of the system without HPF.

In other words, the HPF increases the LF phase margin and the amplitude gain in the midfrequency band. In the proposed method, the amplitude gain at the resonant frequency is suppressed to a very low level, and even if the HPF is added, its amplitude gain is still much less than 0dB. In addition, the HPF can enhance the LF stability, so it is feasible to ignore the HPF when performing stability analysis.

IV. Stability and Parametric Robustness

A. Discrete Model and Stability Analysis

The digital delay in the HSPMSM drive system cannot be ignored, and the current controller is generally designed in the dq synchronous coordinate. Therefore, it is necessary to derive the LCL-equipped HSPMSM discrete synchronous model.

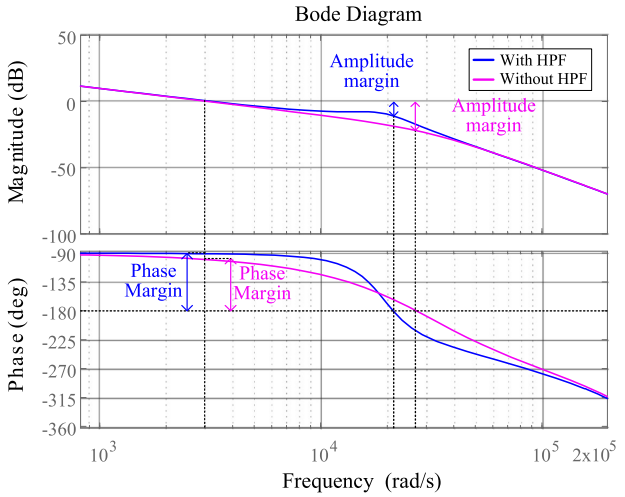

Fig. 13. System Bode plot with and without HPF.

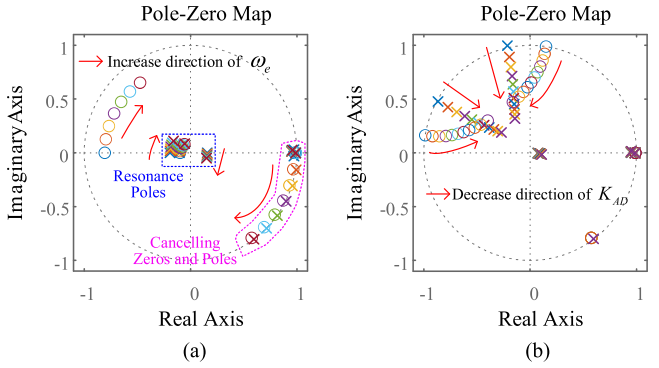

Fig. 14. Closed-loop zero-pole migration diagram. (a) $\omega_e = 0:500\pi:3000\pi$rad, $K_C = -0.3$, $K_{\mathrm{AD}} = -10$. (b) $\omega_e = 3000\pi$rad, $K_C = -0.3$, $K_{\mathrm{AD}} = 0:-0.5-5$.

First, rewrite (19) as

$$G_{i\mathrm{MF}}(s) = \frac{(1+K_C)}{sL_1L_2C}\frac{1}{(s+\varepsilon)^2+\omega_r^2}$$
$$\varepsilon = -K_{\mathrm{AD}}/(2L_2), \omega_r^2 = \bar{\omega}_{\mathrm{res}}^2 - \varepsilon^2. \quad (21)$$

The feedback gain of the damping controller considering harmonic optimization is

$$K_{\mathrm{AD}} = -L_2\bar{\omega}_{\mathrm{res}} - L_2/(2(L_1+L_2)). \quad (22)$$

Perform zero order holder discretization processing on (21), the discrete model in the $\alpha\beta$ rotation coordinate is

$$G_{i\mathrm{MF}}(z) = Z\left[\frac{1-e^{-sT}}{s}G_{i\mathrm{MF}}(s)\right] = \frac{1+K_C}{L_1+L_2}\left[\frac{T}{z-1} - \frac{2\varepsilon}{\bar{\omega}_{\mathrm{res}}^2} + \frac{P_1(z)+P_2(z)}{Q(z)}\right] \quad (23)$$

where T is the LF-VSI sampling period, $P_1(z)$, $P_2(z)$, and $Q(z)$ are defined as

$$P_1(z) = \left(\frac{2\varepsilon}{\bar{\omega}_{\mathrm{res}}^2\omega_r} - \frac{1}{\omega_r}\right)(z-1)e^{-\varepsilon T}\sin(\omega_r T)$$
$$P_2(z) = \frac{2\varepsilon}{\bar{\omega}_{\mathrm{res}}^2}(z-1)(z-\cos(\omega_r T)e^{-\varepsilon T})$$
$$Q(z) = z^2 - 2ze^{-\varepsilon T}\cos(\omega_r T) + e^{-2\varepsilon T}. \quad (24)$$

Considering the digital delay and the dq rotation coordinate transformation [4], the discrete model in the dq synchronous coordinate is

$$G_{i\mathrm{MFr}}(z) = \frac{1+K_C}{L_1+L_2}\frac{1}{z}\left[\frac{T}{ze^{j\omega_e T}-1} - \frac{2\varepsilon}{\bar{\omega}_{\mathrm{res}}^2} + \frac{P_{1r}(z)+P_{2r}(z)}{Q_r(z)}\right] \quad (25)$$

where ω_e is the motor current fundamental angular frequency, $P_{1r}(z)$, $P_{2r}(z)$, and $Q_r(z)$ are defined as

$$P_{1r}(z) = \left(\frac{2\varepsilon}{\bar{\omega}_{\mathrm{res}}^2\omega_r} - \frac{1}{\omega_r}\right)(ze^{j\omega_e T}-1)e^{-\varepsilon T}\sin(\omega_r T)$$
$$P_{2r}(z) = \frac{2\varepsilon}{\bar{\omega}_{\mathrm{res}}^2}(ze^{j\omega_e T}-1)(ze^{j\omega_e T}-\cos(\omega_r T)e^{-\varepsilon T})$$
$$Q_r(z) = z^2e^{2j\omega_e T} - 2ze^{j\omega_e T-\varepsilon T}\cos(\omega_r T) + e^{-2\varepsilon T}. \quad (26)$$

The closed-loop transfer function is

$$G_{\mathrm{closed}}(z) = \frac{G_c(z)G_{i\mathrm{MFr}}(z)}{1+G_c(z)G_{i\mathrm{MFr}}(z)}. \quad (27)$$

The migration diagram of the closed-loop zero-pole points varies with ω_e is shown in Fig. 14(a). The zero-pole migration diagram shows that the system resonant poles rotate clockwise as ω_e increases. It is stable in the range of 0 to 3000πrad and has a large stability margin. Even if ω_e increases further, the system will not become unstable, indicating that the system has good stability in a wide speed range.

In Fig. 14(b), ω_e and K_C are 3000πrad and –0.3, K_{AD} decreases gradually from 0 to –5. The analysis results show that when $K_{\mathrm{AD}} = 0$, the closed-loop poles are not all located within the unit circle and the system is unstable. As K_{AD} decreases,

$$G_{i\mathrm{MFH}}(s) = \frac{1+K_CG_{\mathrm{HPF}}(s)}{s^3L_1L_2C + s(L_1+L_2)(1+K_CG_{\mathrm{HPF}}(s)) - s^2L_1CK_{\mathrm{AD}}G_{\mathrm{HPF}}(s)}$$

$$= \frac{s(1+K_C)+\omega_c}{s^4L_1L_2C + s^3(L_1L_2C\omega_c - L_1CK_{\mathrm{AD}}) + s^2(L_1+L_2)(1+K_C) + s(L_1+L_2)\omega_c}. \quad (20)$$

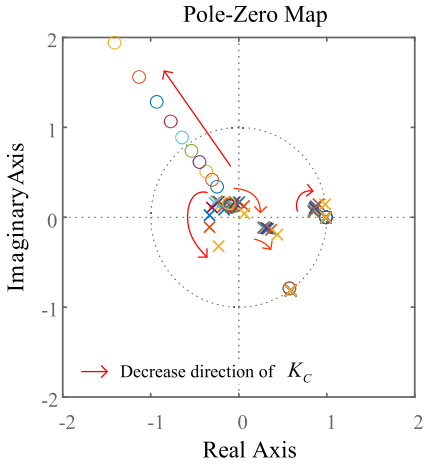

Fig. 15. Relationship between closed-loop zero and pole and K_C, $K_C = 0 : -0.1 - 0.9$, $\omega_e = 3000\pi$rad.

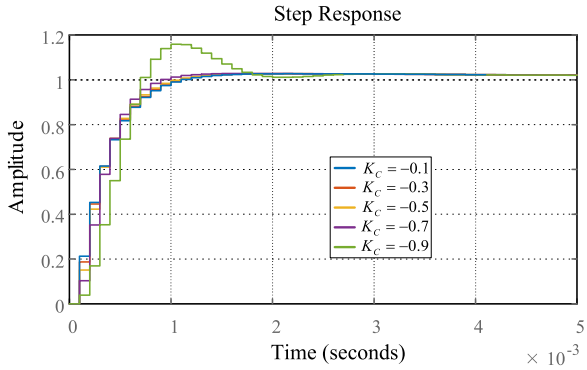

Fig. 16. Step response with K_C, $\omega_e = 3000\pi$rad.

the closed-loop resonant zero poles gradually move inside the circle, and the stability margin of the system gradually increases.

B. Harmonic Optimization Controller Gain Selection

It is worth noting that one of the zero points of the closed-loop system is close to the edge of the unit circle in Fig. 14(a). If K_C changes, the zero point may move away from the unit circle, which will deteriorate the system dynamic performance.

It can be seen from (18), K_C should be less than zero and greater than –1

$$K_C \in (-1, 0)\,. \tag{28}$$

Fig. 15 describes the closed-loop zero-pole distribution of the system with different K_C, the range of K_C is –0.9 to 0. The analysis results show that K_C has little effect on the poles, but a great impact on the zeros. The step response results are shown in Fig. 16. Although the position of the zero point does not affect the stability of the system, a zero point far away from the origin will increase the dynamic overshoot of the system.

In summary, the larger the absolute value of K_C is, the stronger the harmonic optimization capability is, but it will deteriorate the dynamic performance and increase the damper

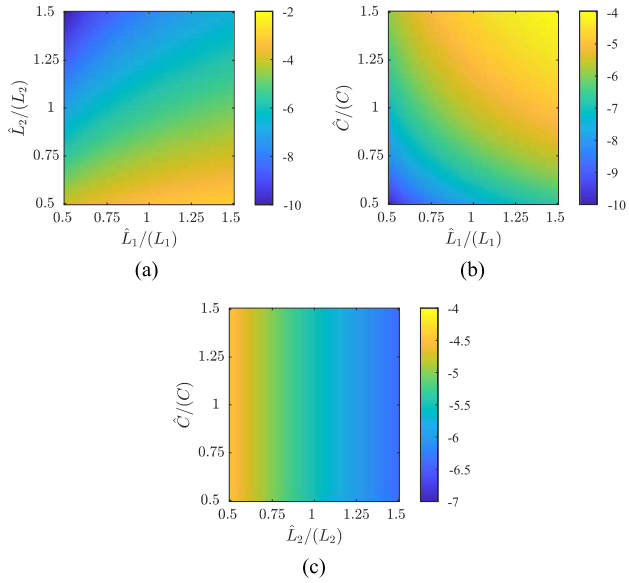

Fig. 17. Impact of system parameter mismatch on K_{AD}, $K_C = -0.7$, K_{AD} with ideal parameter is -5.48. (a) $\hat{L}_1 = (0.5 - 1.5)L_1$, $\hat{L}_2 = (0.5 - 1.5)L_2$, $\hat{C} = C$. (b) $\hat{L}_1 = (0.5 - 1.5)L_1$, $\hat{C} = (0.5 - 1.5)C$, $\hat{L}_2 = L_2$. (c) $\hat{L}_2 = (0.5 - 1.5)L_2$, $\hat{C} = (0.5 - 1.5)C$, $\hat{L}_1 = L_1$.

loss. To take both into account, the recommended K_C range is

$$K_C \in [-0.7, -0.4]\,. \tag{29}$$

C. Parameter Robustness Analysis

It can be seen from (22) that the value of the feedback gain is affected by parameter mismatch. Further analysis shows that the parameters that affect the stability of the system are inductance L_1, capacitance C, and inductance L_2. For ease of description, the mismatch parameters are recorded as $\hat{L}_1$, $\hat{C}$, and $\hat{L}_2$, respectively. Generally speaking, in motor drives, the allowable error of filter component parameters is $\pm 20\%$, and the allowable error of motor inductance is $\pm 50\%$ [4].

As shown in Fig. 17, K_{AD} is affected by three parameters, $\hat{L}_1$, $\hat{L}_2$, and $\hat{C}$. If the system parameters are actual parameters, K_{AD} is approximately –5.48. When the system parameters vary from 0.5 to 1.5 times the actual parameters, the range of K_{AD} is about –10 to –2.

It can be seen from Fig. 14(b) that when K_{AD} is not greater than –0.5, all the closed-loop poles of the system are located within the unit circle and the system is stable. In the parameter robustness analysis, the maximum value of K_{AD} is –2, which is less than –0.5. Therefore, the proposed method has good parameter robustness.

V. Experimental Validations

The experimental setup is shown in Fig. 18. The main components of the experimental platform are dual three-phase HSPMSM, LF-VSI with *LC* filter, HF-Damper, three-phase load resistors, oscilloscopes, dc power supply. The experimental plant parameters aligned with those in Table II. The HSPMSM is a ten-pole, dual three-phase surface-mounted motor with a rated speed

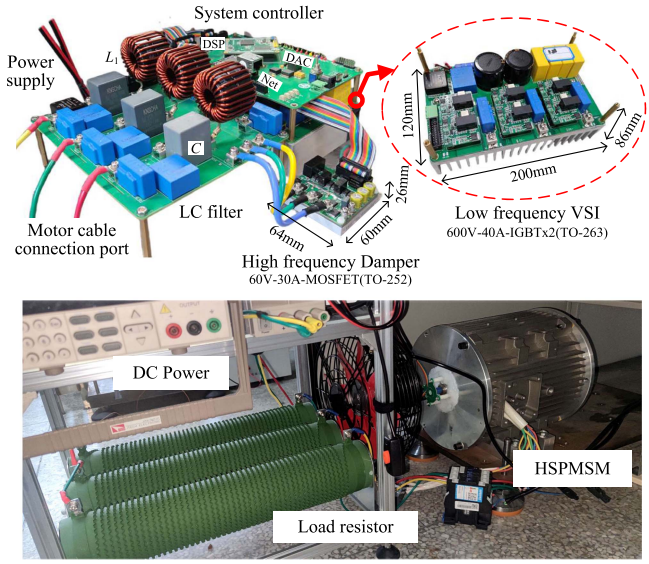

Fig. 18. Experimental setup.

TABLE III
PARAMETERS OF SYSTEM CONTROLLER

Controller	Description	Parameter	Value
Motor current controller	Control coefficient	a b	0.5 −0.49
Damper dc-link voltage controller	Proportional coefficient integral coefficient	K_{pV} K_{iV}	0.6 1
Motor speed controller	Proportional coefficient integral coefficient	K_{pS} K_{iS}	0.01 0.02

TABLE IV
FILTER PARAMETERS FOR EXPERIMENTAL VERIFICATION

	L_1	L_2	C	f_{res}
LCL filter-A	200 μH	220 μH	8 μF	5498 Hz
LCL filter-B	100 μH	220 μH	8 μF	6786 Hz

of 12 kr/min. A set of three-phase windings of the HSPMSM is connected to the three-phase load resistor, so the load torque is proportional to the speed. The switching device of the LF-VSI is two parallel 600 V–40 A IGBTs (STGF19NC60HD packaged in TO-263), and the switching device used by the HF-Damper is a single-tube MOSFET of 60 V–30 A (UMW30N06 packaged in TO-252). The control unit is digital signal processor TMS32F28377D and the clock frequency is 200 MHz. The parameters of the system controller are shown in Table III. The two filters shown in Table IV are experimental objects. Filter-A is used for high-speed conditions, and filter-B is used for low-speed conditions.

A. Resonance Damping Verification

In this section, the gain of the harmonic optimization controller is set to 0. The damping verification experimental results are shown in Fig. 19, where i_{a_M} is the motor A-phase current, i_{a_HF} is the HF damper A-phase current, i_{a_LF} is the LF inverter A-phase current, and speed indicates the motor speed in r/min.

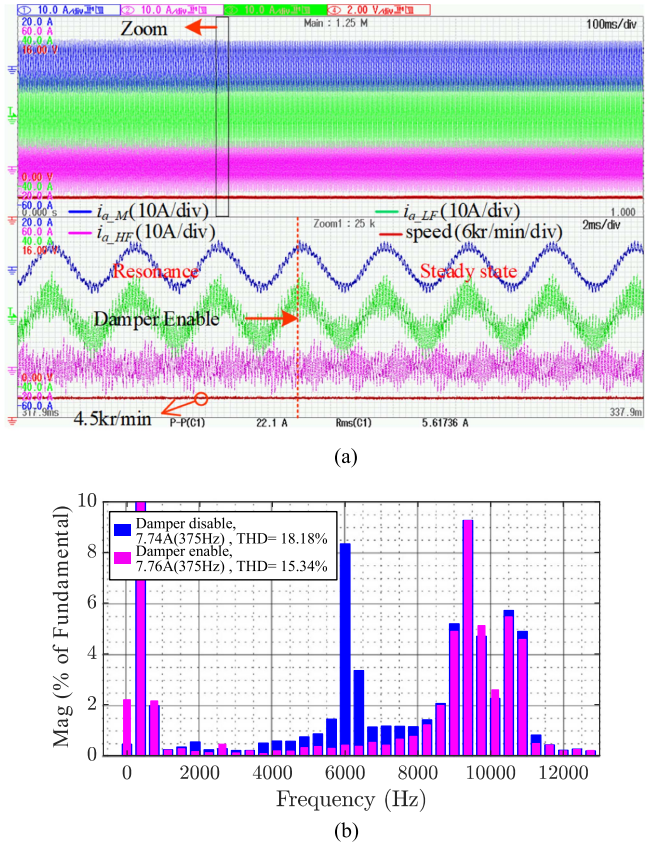

Fig. 19. Validity verification experimental results with filter-B. (a) Damper switching process results at 4.5 kr/min. (b) FFT of motor phase current.

Fig. 19(a) shows the motor phase current waveforms before and after the damper is enabled. The fast Fourier transform (FFT) result of i_{a_M}, as shown in Fig. 19(b), indicates that the HF-Damper reduces the total harmonic distortion (THD) of the motor current from 18.18% to 15.34%, and reduces the harmonic amplitude at the resonant frequency from 8.5% of the fundamental amplitude to about 0.2% of the fundamental amplitude. The experimental results show that the proposed method is an effective means to suppress resonance.

The speed step experiment results are shown in Fig. 20, the speed reference steps from 3 to 12 kr/min. The definition of channel variable is the same as Fig. 19. The motor phase current THD at 12 kr/min is 15.50%. The experimental results demonstrate that the test motor operates stably under speed step conditions with the proposed method.

Fig. 21 shows the experimental results of the HF-Damper rotor position θ_{HF} obtained by recursion of the LF-VSI rotor position θ and angular frequency ω_e, the speed is 12 kr/min. The experimental results show that using the recursive method in (14), high-precision rotor position can be obtained even when there is only an LF rotor position observer.

B. DC-Link Voltage Control

The HF damper dc-link voltage control experimental results are presented in Figs. 22 and 23, where U_{VC} is the output of the voltage controller, V_{dc2} is the damper dc link voltage. The

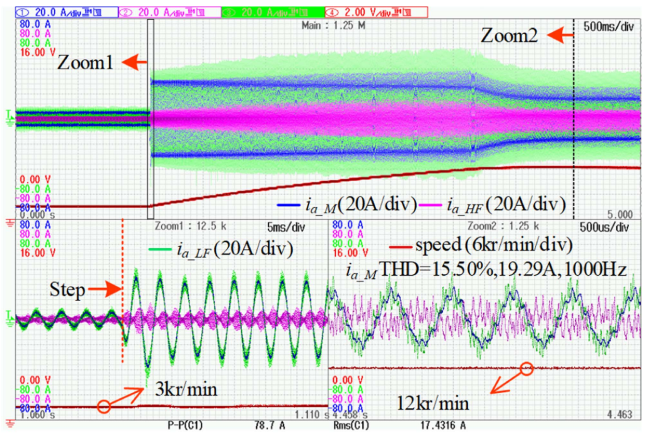

(a)

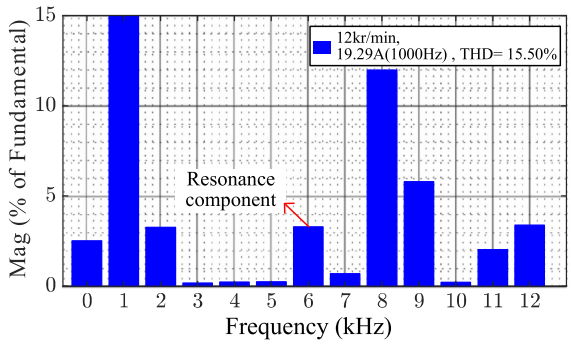

(b)

Fig. 20. Speed step experimental results with filter-A: 3–12 kr/min. (a) Experimental waveform. (b) Motor current FFT results at 12 kr/min.

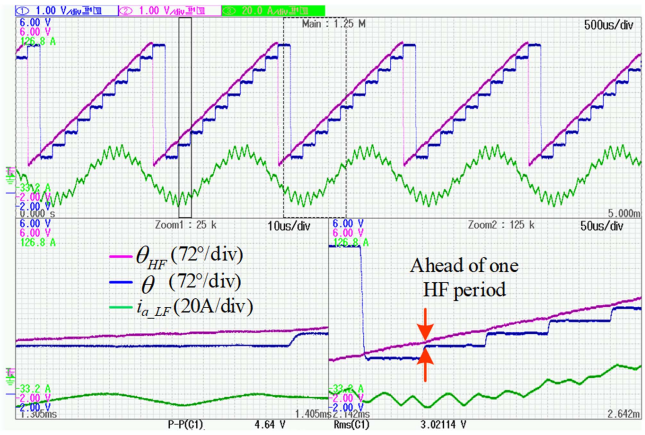

Fig. 21. HF-Damper rotor position recursion results with filter-A.

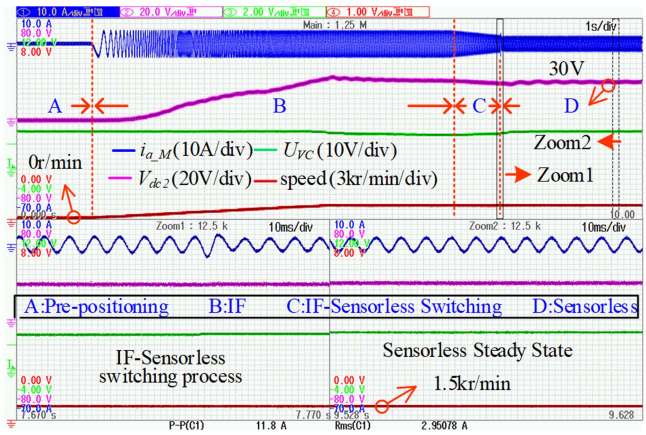

Fig. 22. HF-Damper DC-link capacitor precharging experimental results.

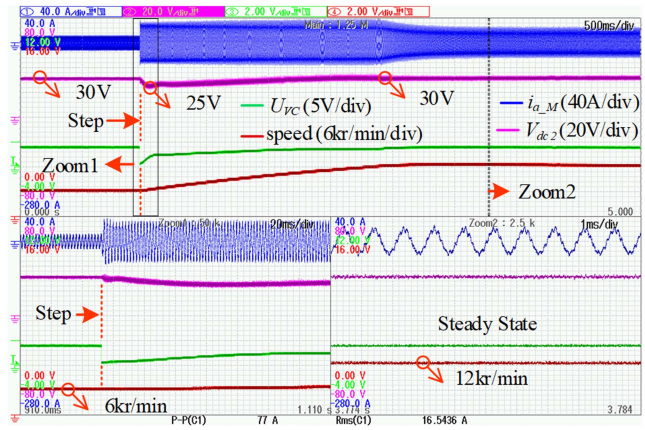

(a)

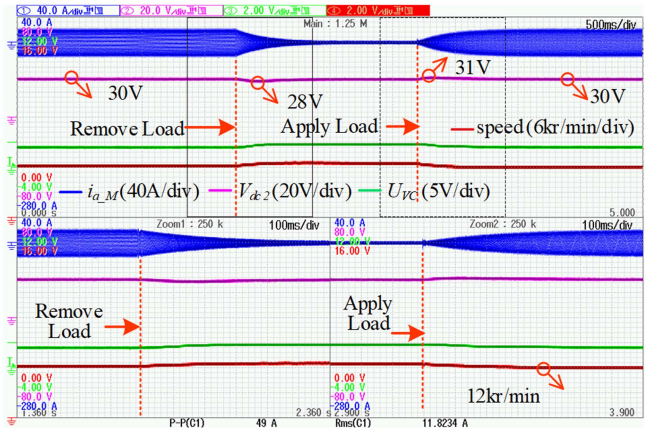

(b)

Fig. 23. HF-Damper DC-link voltage control experimental results. (a) Speed step, 6 to 12 kr/min. (b) Load step.

damper dc-link capacitor is precharged during the motor starting process. As shown in Fig. 22, the starting method adopted is a typical three-stage method, including prepositioning, constant current variable frequency acceleration (IF), and sensorless switching. Since resonance is not prominent at low speeds, the resonance damping controller is disabled during the startup process. The target speed of IF is 1.5 kr/min. After the speed stabilizes, the current amplitude gradually decreases to reduce the difference between the open-loop position and the observer position, facilitating a smooth switch to the sensorless control mode.

The experimental results shown in Fig. 22 show that the HF damper capacitor voltage gradually increases in the IF stage and

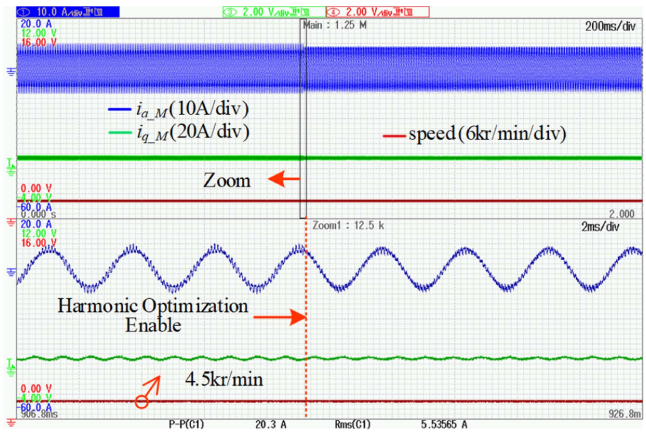

(a)

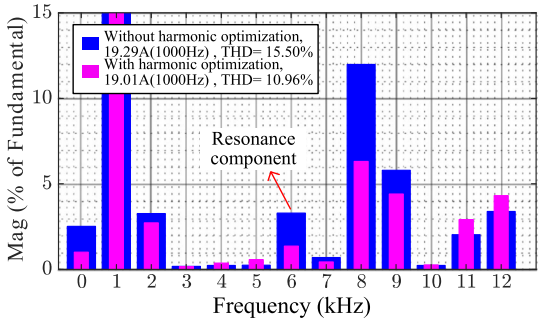

(b)

Fig. 24. Harmonic optimization experimental results with filter-B at 4.5 kr/min. (a) Harmonic optimization switching process. (b) FFT of motor phase current.

finally reaches the given value of 30 V after the motor is switched into the sensorless control state.

The experiments shown in Fig. 23 is to observe how the dynamics of the motor relate to the dynamics of the HF damper dc voltage. Fig. 23(a) tests the control performance of the damper dc voltage when the motor speed steps from 6 to 12 kr/min. During the speed step process, the damper capacitor voltage first drops from 30 to 25 V, and then recovers to 30 V. The experimental results show that the damper voltage control has good performance under the speed step condition. Fig. 23(b) tests the control performance of the damper dc voltage when a rated load is given and removed from the motor. After the load is removed, the damper dc voltage first drops to 28 V and then recovers to 30 V. After the load is reapplied, the damper dc voltage rises slightly and then recovers to 30 V.

C. Harmonic Optimization Verification

Fig. 24(a) shows the experimental waveform of the switching process of the harmonic optimization controller at 4.5 kr/min, and K_C is –0.7. As shown in Fig. 24(b), before the harmonic optimization controller is enabled, the THD of the motor phase current is 15.26%. After enabling the harmonic optimization controller, the motor current THD is reduced to 11.09%.

In Fig. 25, the motor speed increases to 12 kr/min. i_{c_HF} is the HF-Damper C-phase current. As shown in Fig. 25(b),

TABLE V
RELATIONSHIP BETWEEN K_C AND SYSTEM PERFORMANCE

K_C	−0.1	−0.3	−0.5	−0.7	−0.9
i_{a_M} THD (%)	15.11	13.13	11.74	10.96	11.12
i_{q_M} Overshoot (A)	8.1	8.2	8.5	8.8	12.3

TABLE VI
COMPARISON RESULTS OF DIFFERENT DAMPING METHODS WITH FILTER-A

	PD	CCF	Proposed damping only	Proposed
Total power (W)	3016	3002	2990	2903
Damping loss (W)	29.4	Unknown	Unknown	Unknown
i_{a_M} THD (%)	15.06	19.33	15.50	10.96

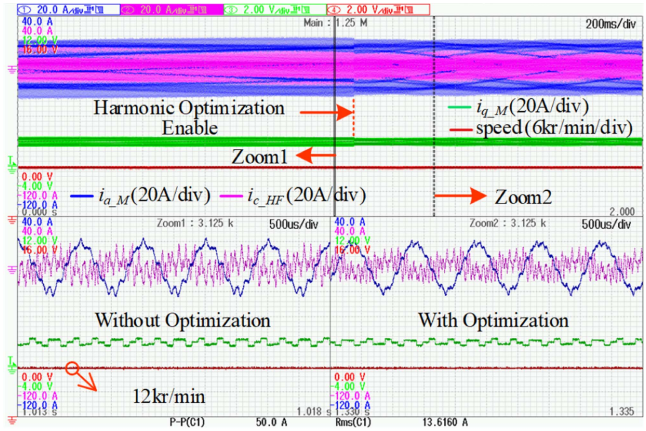

(a)

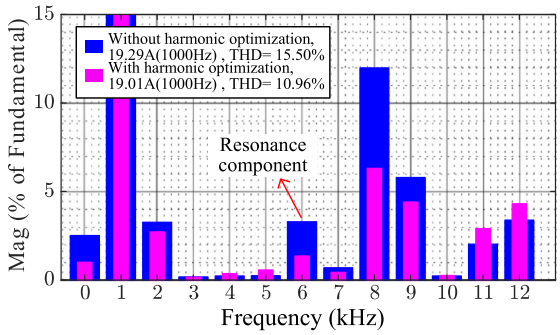

(b)

Fig. 25. Harmonic optimization experimental results with filter-A at 12 kr/min. (a) Harmonic optimization switching process. (b) FFT of motor phase current.

the proposed harmonic optimization method reduces the motor current THD from 15.50% to 10.96%. It is worth noting that the proposed harmonic optimization method reduces the phase current of the HF-Damper from 7.35 to 6.26 A in Fig. 25(a), a decrease of 15%. In this section, the resonance damping controller remains enabled to suppress the resonance. Figs. 24 and 25 are the experimental results of harmonic optimization function verification with filter-B and filter-A, respectively.

In order to explore the impact of KC on system performance, K_C was selected as –0.1, –0.3, –0.7, and –0.9 for testing. The experimental results are shown in Table V. The experimental results show that when K_C is greater than –0.7, as K_C decreases,

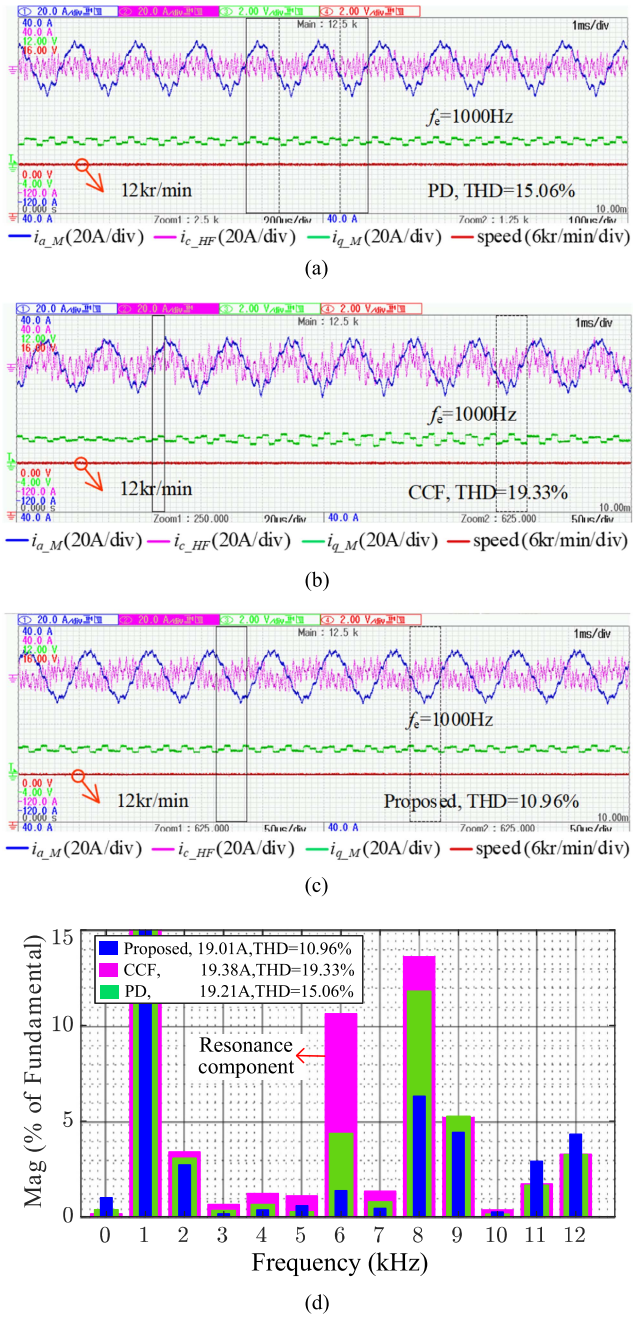

Fig. 26. Comparative experimental results of different damping methods with filter-A at 12 kr/min. (a) PD method in [5]. (b) CCF method in [32]. (c) Proposed method. (d) Motor current THD.

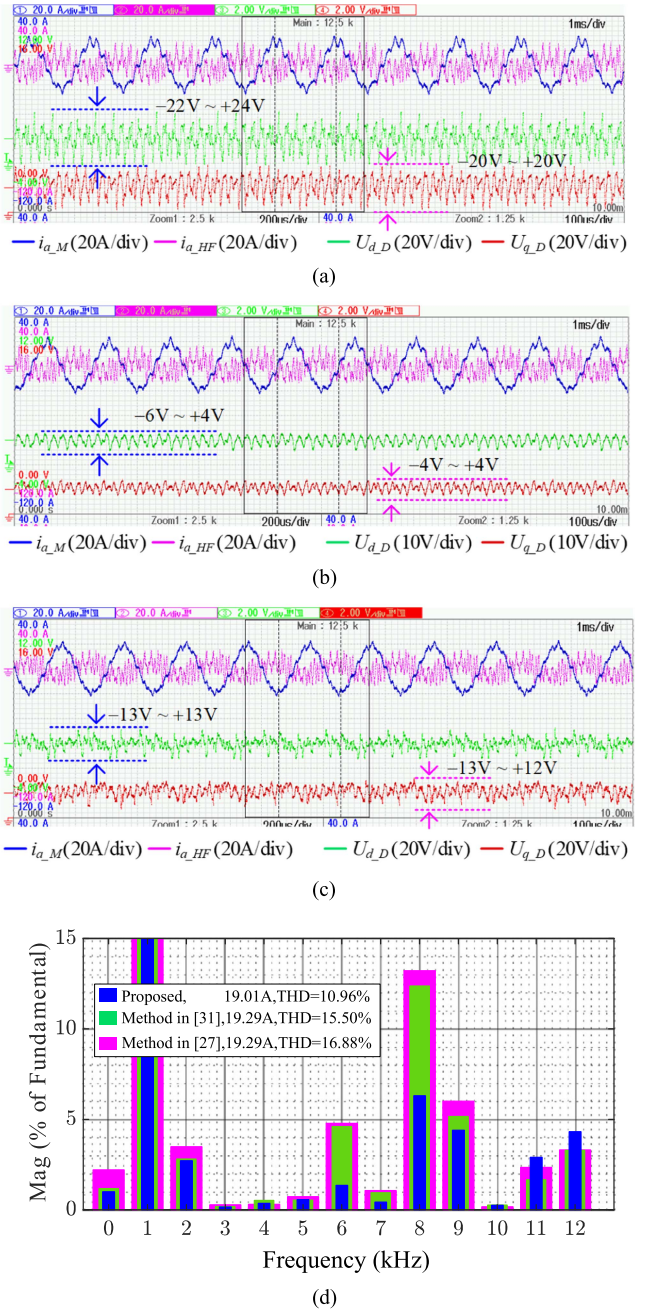

Fig. 27. Comparison of experimental results with existing active damper with filter-A. (a) Multicurrent feedback method in [27], V_{dc2} is 80 V. (b) Single-motor-current feedback method in [31], V_{dc2} is 15 V. (c) Proposed method, V_{dc2} is 30 V. (d) Motor current THD.

the overshoot of i_{q_M} increases slowly, the motor current THD decreases gradually, and the decline rate of motor current THD gradually becomes smaller. But if K_C is –0.9, the motor current THD increases instead, and the overshoot of i_{q_M} become much larger. The reason may be that the damper output voltage exceeds the limit.

D. Comparison With Other Damping Methods

In this section, capacitive branch series resistor PD method in [5] and CCF method in [32] are compared with the proposed method. The PD resistor is selected based on the principle that the amplitude gain of the damped system at the resonant frequency is equal to 1. The expression of R_d with filter-A is

$$R_d = \sqrt{\frac{1}{\frac{(L_1+L_2)^4}{L_1^2L_2^2} - \frac{L_1+L_2}{L_1L_2}C}} = 0.25. \tag{30}$$

The comparative experimental results of the system equipped with filter-A are presented in Table VI and Fig. 26. The speed reference is 12 kr/min to keep the load power the same.

TABLE VII
PARAMETER MISMATCH EXPERIMENTAL RESULTS WITH FILTER-A AT 12 KR/MIN, $K_C = -0.7$

	Exp.A	Exp.B	Exp.C	Exp.D	Exp.E	Exp.F	Exp.G	Exp.H
$\hat{L}_1(L_1)$	0.5	0.5	0.5	0.5	1.5	1.5	1.5	1.5
$\hat{L}_2(L_2)$	0.5	0.5	1.5	1.5	0.5	0.5	1.5	1.5
$\hat{C}(C)$	0.5	1.5	0.5	1.5	0.5	1.5	0.5	1.5
K_{AD}	–4.42	–2.67	–10.78	–6.34	–3.49	–2.07	–7.47	–4.42
i_{a_M} THD (%)	11.03	11.31	10.47	10.71	11.15	11.23	10.66	10.99

In the PD system, the motor current amplitude is 19.21 A, the motor current THD is 15.06%, the total power is 3016 W, and the power consumed by the damping resistor is about 30 W. Therefore, it can be concluded that the total power without damping loss is 2986 W. The PD method can effectively suppress resonance, but the power consumed by the damping resistor is high.

In the CCF system, the motor current amplitude is 19.38 A, the motor current THD is 19.33%, the total power is 3002 W. The resonant frequency of filter-A has exceeded the Nyquist frequency of the system, so the CCF method cannot effectively suppress the resonance. The loss caused by resonance is about 16 W.

In the system with the proposed resonance damping and harmonic optimization methods, the motor current amplitude is 19.01 A, the motor current THD is 10.96%, the total power is 2903 W. The proposed harmonic optimization method reduces the system power by 87 W (2.91%) compared to the method using only the resonant damping controller. Compared with the PD method, the proposed method has a power consumption of 113 W lower (3.75%).

The comparative experimental results with the existing damper are shown in Fig. 27, which shows the experimental results of the multicurrent feedback method in [27], the single current feedback method in [31], the proposed method, and the comparison chart of the motor current FFT analysis results of the three methods. It is important to point out that the damper used in the multiple current feedback method is a high voltage version (600 Vdc). The experiment was carried out in the speed control mode with a reference speed of 12 kr/min. U_{q_D} and U_{d_D} are resonance damping controller output d- and q-axis voltage.

The experimental results show that the multicurrent feedback method has the highest THD of 16.88%, and its damper output voltage is also the highest. Therefore, this method is not recommended. The single current feedback method has the lowest damper output voltage, and the motor current THD is slightly better than the multipoint feedback method, ranking in the middle. The proposed method has the lowest motor current THD of 10.96%, and the damper output voltage range ranks in the middle. Compared with the single current feedback method, the proposed method uses a higher damper voltage (increased from 15 to 30 V) in exchange for a lower motor current THD, which reduces the motor loss by about 87 W (2.91%).

E. Parameter Robustness Verification

The parameter robustness experimental results with filter-A are summarized in Table VII. For the mismatch parameter ($\hat{L}_1$, $\hat{L}_2$, and $\hat{C}$), the upper and lower bounds of the preset range were selected respectively, and a total of eight groups of experiments, Exp.A to Exp.H, are carried out. The speed reference is 12 kr/min and K_C is –0.7.

In the experiments described previously, the mismatched parameters cause the resonant damping feedback gain K_{AD} (–4.42 with ideal parameters) to vary from –10.78 to –2.0. The THD of the motor current in different experiments is slightly different, with a distribution range of 10.66%–11.31%. Experimental results show that the proposed method can tolerate 50% error in system parameters.

VI. CONCLUSION

This article extends the harmonic optimization capabilities of capacitively coupled active dampers for LCL-equipped HSPMSM drives. Based on the resonant damping method of motor current feedback, capacitor voltage state feedback is added to further reduce the motor current harmonics. Compared with the single current sensor control method, the damper output voltage is higher, but it also brings the following benefits.

1) Reduce the motor current THD by more than 25%.
2) Reduce the HF-Damper current by about 15%.
3) Improve the system efficiency by about 3%.

REFERENCES

[1] D. Gerada, A. Mebarki, N. L. Brown, C. Gerada, A. Cavagnino, and A. Boglietti, "High-speed electrical machines: Technologies, trends, and developments," *IEEE Trans. Ind. Electron.*, vol. 61, no. 6, pp. 2946–2959, Jun. 2014.

[2] Z. Zhu, J. Deng, H. Ouyang, and X. Dou, "Optimized sampling mechanism for full-state feedback current control of LCL-Equipped high-speed PMSMs for fuel cell air compressor," *IEEE Trans. Transport. Electrific.*, vol. 9, no. 2, pp. 3386–3397, Jun. 2023.

[3] K. K.-F. Yuen and H. S.-H. Chung, "A low-loss "RL-Plus-C" filter for overvoltage suppression in inverter-fed drive system with long motor cable," *IEEE Trans. Power Electron.*, vol. 30, no. 4, pp. 2167–2181, Apr. 2015.

[4] Y. Yao, Y. Huang, F. Peng, J. Dong, and Z. Zhu, "Dynamic-decoupled active damping control method for improving current transient behavior of LCL-Equipped high-speed PMSMs," *IEEE Trans. Power Electron.*, vol. 37, no. 3, pp. 3259–3271, Mar. 2022.

[5] R. N. Beres, X. Wang, M. Liserre, F. Blaabjerg, and C. L. Bak, "A review of passive power filters for three-phase grid-connected voltage-source converters," *IEEE Trans. Emerg. Sel. Topics Power Electron.*, vol. 4, no. 1, pp. 54–69, Mar. 2016.

[6] W. Yao, Y. Yang, X. Zhang, F. Blaabjerg, and P. C. Loh, "Design and analysis of robust active damping for LCL filters using digital notch filters," *IEEE Trans. Power Electron.*, vol. 32, no. 3, pp. 2360–2375, Mar. 2017.

[7] E. Rodriguez-Diaz, F. D. Freijedo, J. C. Vasquez, and J. M. Guerrero, "Analysis and comparison of notch filter and capacitor voltage feedforward active damping techniques for LCL grid-connected converters," *IEEE Trans. Power Electron.*, vol. 34, no. 4, pp. 3958–3972, Apr. 2019.

[8] J. Wang, J. D. Yan, L. Jiang, and J. Zou, "Delay-dependent stability of single-loop controlled grid-connected inverters with LCL filters," *IEEE Trans. Power Electron.*, vol. 31, no. 1, pp. 743–757, Jan. 2016.

[9] X. Wang, C. Bao, X. Ruan, W. Li, and D. Pan, "Design considerations of digitally controlled LCL-Filtered inverter with capacitor- current-feedback active damping," *IEEE Trans. Emerg. Sel. Topics Power Electron.*, vol. 2, no. 4, pp. 972–984, Dec. 2014.
[10] X. Wang, F. Blaabjerg, and P. C. Loh, "Virtual RC damping of LCL-Filtered voltage source converters with extended selective harmonic compensation," *IEEE Trans. Power Electron.*, vol. 30, no. 9, pp. 4726–4737, Sep. 2015.
[11] S. G. Parker, B. P. McGrath, and D. G. Holmes, "Regions of active damping control for LCL filters," *IEEE Trans. Ind. Appl.*, vol. 50, no. 1, pp. 424–432, Jan./Feb. 2014, doi: 10.1109/TIA.2013.2266892.
[12] G. G. Koch, L. A. Maccari, R. C. L. F. Oliveira, and V. F. Montagner, "Robust $\mathcal{H}_\infty$ state feedback controllers based on linear matrix inequalities applied to grid-connected converters," *IEEE Trans. Ind. Electron.*, vol. 66, no. 8, pp. 6021–6031, Aug. 2019.
[13] Y. He, X. Wang, X. Ruan, D. Pan, and K. Qin, "Hybrid active damping combining capacitor current feedback and point of common coupling voltage feedforward for LCL-Type grid-connected inverter," *IEEE Trans. Power Electron.*, vol. 36, no. 2, pp. 2373–2383, Feb. 2021.
[14] Y. Lei, W. Xu, C. Mu, Z. Zhao, H. Li, and Z. Li, "New hybrid damping strategy for grid-connected photovoltaic inverter with LCL filter," *IEEE Trans. Appl. Supercond.*, vol. 24, no. 5, Oct. 2014, Art. no. 0601608.
[15] M. A. Awal, L. D. Flora, and I. Husain, "Observer based generalized active damping for voltage source converters with LCL filters," *IEEE Trans. Power Electron.*, vol. 37, no. 1, pp. 125–136, Jan. 2022, doi: 10.1109/TPEL.2021.3093504.
[16] Y. Yao, Y. Huang, F. Peng, J. Dong, and Z. Zhu, "A general single-sensor damping framework for LCL-Equipped high-speed PMSM drives," *IEEE Trans. Ind. Electron.*, vol. 70, no. 5, pp. 5375–5380, May 2023, doi: 10.1109/TIE.2022.3186342.
[17] S. Liu, Q. Wang, G. Zhang, G. Wang, and D. Xu, "Online temperature identification strategy for position sensorless PMSM drives with position error adaptive compensation," *IEEE Trans. Power Electron.*, vol. 37, no. 7, pp. 8502–8512, Jul. 2022.
[18] Q. Wang, G. Wang, N. Zhao, G. Zhang, Q. Cui, and D. Xu, "An impedance model-based multiparameter identification method of PMSM for both offline and online conditions," *IEEE Trans. Power Electron.*, vol. 36, no. 1, pp. 727–738, Jan. 2021.
[19] Z. Ni, Y. Cheng, J. Xu, H. Cheng, J. Zhou, and S. Bai, "An adaptive series active damper for stabilizing grid-connected system under weak grid," in *Proc. 2021 4th Int. Conf. Energy, Elect. Power Eng.*, Chongqing, China, Apr. 2021, pp. 581–586.
[20] L. Jia, X. Ruan, W. Zhao, Z. Lin, and X. Wang, "An adaptive active damper for improving the stability of grid-connected inverters under weak grid," *IEEE Trans. Power Electron.*, vol. 33, no. 11, pp. 9561–9574, Nov. 2018.
[21] X. Wang, F. Blaabjerg, M. Liserre, Z. Chen, J. He, and Y. Li, "An active damper for stabilizing power-electronics-based AC systems," *IEEE Trans. Power Electron.*, vol. 29, no. 7, pp. 3318–3329, Jul. 2014.
[22] Q. Jin, Z. Yao, and M. Guo, "Stability improvement for multi-inverter system based on active damper with modified resonance detection method," in *Proc. 2020 4th Int. Conf. HVDC*, Nov. 2020, pp. 326–331.
[23] Z. Lin and X. Ruan, "A three-phase adaptive active damper for improving the stability of grid-connected inverters under weak grid," in *Proc. 2019 IEEE Appl. Power Electron. Conf. Expo.*, Anaheim, CA, USA, Mar. 2019, pp. 1084–1089.
[24] X. Wang, F. Blaabjerg, and M. Liserre, "An active damper to suppress multiple resonances with unknown frequencies," in *Proc. 2014 IEEE Appl. Power Electron. Conf. Expo.*, Fort Worth, TX, USA, Mar. 2014, pp. 2184–2191.
[25] W. Zhou, F. Li, X. Zhang, P. Liu, J. Xu, and Y. Liu, "Voltage source active damper applied to resonance suppression of multi-inverter grid-connected," in *Proc. 2018 IEEE Int. Power Electron. Appl. Conf. Expo.*, Nov. 2018, pp. 1–6.
[26] X. Wang, Y. Pang, P. C. Loh, and F. Blaabjerg, "A Series-LC-Filtered active damper with grid disturbance rejection for AC power-electronics-based power systems," *IEEE Trans. Power Electron.*, vol. 30, no. 8, pp. 4037–4041, Aug. 2015.
[27] H. Bai, X. Wang, P. C. Loh, and F. Blaabjerg, "An active trap filter for switching harmonic attenuation of low-pulse-ratio inverters," *IEEE Trans. Power Electron.*, vol. 32, no. 12, pp. 9078–9092, Dec. 2017.
[28] H. Bai, X. Wang, F. Blaabjerg, and P. C. Loh, "Harmonic analysis and mitigation of low-frequency switching voltage source inverter with auxiliary VSI," *IEEE Trans. Emerg. Sel. Topics Power Electron.*, vol. 6, no. 3, pp. 1355–1365, Sep. 2018.
[29] H. Bai, X. Wang, P. C. Loh, and F. Blaabjerg, "Harmonic analysis and mitigation of low-frequency switching voltage source inverter with series LC filtered VSI," in *Proc. 2017 IEEE Appl. Power Electron. Conf. Expo.*, Tampa, FL, USA, Mar. 2017, pp. 3299–3306.
[30] J. Zhou, F. Pen, Y. Huang, and Y. Yao, "Capacitively coupled active resonant damper for HSPMSM equipped with LCL filter," in *Proc. 2024 IEEE 33rd Int. Symp. Ind. Electron.*, Jun. 2024, pp. 1–6.
[31] J. Zhou, F. Peng, Y. Huang, and Y. Yao, "Single-motor-Current feedback resonance damping method for LCL-Equipped HSPMSMs based on capacitively coupled active damper," *IEEE Trans. Power Electron.*, vol. 39, no. 12, pp. 16458–16470, Dec. 2024, doi: 10.1109/TPEL.2024.3443656.
[32] X. Li, X. Wu, Y. Geng, X. Yuan, C. Xia, and X. Zhang, "Wide damping region for LCL-Type grid-connected inverter with an improved capacitor-current-feedback method," *IEEE Trans. Power Electron.*, vol. 30, no. 9, pp. 5247–5259, Sep. 2015.
[33] S. C. Yang and G. R. Chen, "High-speed position-sensorless drive of permanent-magnet machine using discrete-time EMF estimation," *IEEE Trans. Ind. Electron.*, vol. 64, no. 6, pp. 4444–4453, Jun. 2017.

Jiaxin Zhou (Student Member, IEEE) received the B.S. degree from East China Jiaotong University, Nanchang, China, in 2018, and the M.S. degree from Hunan University, Changsha, China, in 2021, both in electrical engineering. He is currently working toward the doctor of engineering degree in electric machines and control with the School of Electrical Engineering, Southeast University, Nanjing, China.

His research interests include the current regulator design and sensorless control of high-speed PMSM.

Yunkai Huang received the M.Sc. and Ph.D. degrees in electrical engineering from Southeast University, Nanjing, China, in 2001 and 2007, respectively.

He is currently a Professor with the School of Electrical Engineering, Southeast University. His research interests include design and control of PM machine and high-speed machine, applications in domestic appliances, electric vehicles, railway traction, all-electric ships, more-electric aircraft, and wind power generation systems.

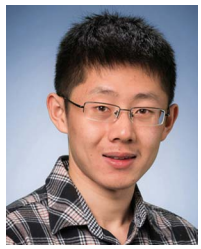

Fei Peng received the B.S. and M.S. degrees in electrical engineering from Southeast University, Nanjing, China, in 2010 and 2012, respectively, and the Ph.D. degree in electrical and computer engineering from McMaster University, Hamilton, ON, Canada, in 2016.

He is currently an Associate Professor with the School of Electrical Engineering. He was a Postdoctoral Fellow with the McMaster Institute for Automotive Research and Technology, McMaster University. Since December 2016, he was with Southeast University. His research interests include optimal design and control of power converters, modeling, and digital control of motor drives.

Yu Yao (Member, IEEE) received the B.S. and Ph.D. degrees in electrical engineering from Southeast University, Nanjing, China, in 2016 and 2022, respectively.

He was an Assistant Professor with the School of Electrical Engineering, Southeast University. His research interests include the design of the power inverter, the current regulator design, the position sensorless drive for the high-speed PMSM and the drive system with LCL output filter.